

Declining short-term emission control opportunity for major events in Chinese cities

Received: 29 August 2024

Accepted: 7 February 2025

Published online: 28 April 2025

 Check for updates

Hanying Wang¹, Qin He², Hao Kong³, Kai Qin², Bo Zheng^{4,5}, Jintai Lin^{6,3} & Yu Zhao^{6,1,6}✉

In China, short-term emission controls have been implemented widely in the host and nearby cities of major events to reduce air pollution. However, insufficient analysis of their effectiveness has weakened the design of pollution controls. In this study, we analyzed the impact of short-term controls on nitrogen oxide emissions and quantified their main drivers in both the host and neighboring cities of 11 events held in east China from 2010 to 2023. We found that short-term controls might be more effective in neighboring cities than in host cities for some events, and that their benefits in terms of reduced emissions have weakened over time. Furthermore, the main sector of emission abatement for events has shifted from power to industry and transportation, reflecting the evolution of emission controls and the relative dominance of air-pollution budgets for different sectors. Our analysis highlights the enhanced targeting of short-term air pollution controls for Chinese cities, which also supports the long-term policy design.

Air pollution, concomitant with the rapid growth of the economy and energy consumption, has long been a major concern in Chinese cities. For the past decade, China has been making great efforts to improve air quality through long-term regulatory frameworks^{1,2}. Meanwhile, developed Chinese cities have hosted a number of major international and domestic events, including the Beijing Olympic Games (August 2008), the Shanghai World Expo (May–October 2010), the Nanjing Youth Olympics (August 2014) and the Hangzhou Asian Games (September–October, 2023). To ensure the smooth operation of these events and to minimize the health risks associated with air pollution, stringent short-term emission control measures were implemented in the host cities of the events on top of the regular national policies on air quality^{3–8}. Moreover, neighboring cities were usually also required to take

additional measures (probably not as stringent as in the host cities) to achieve regional joint control of air pollution⁹. Typically, these measures included the temporary closure of manufacturing plants, the implementation of enhanced emission standards in the industrial and power sectors, the prohibition of certain residential and commercial activities, and traffic restrictions in specific urban areas. These were initiated before individual events, gradually tightened and maintained during the event, and lifted after the event, resulting in declining air pollutant concentration during the event^{4,5}. These short-term controls can be considered as ‘large-scale social experiments’ to examine the instant response of air quality to human activities, offer valuable information on urban air quality improvement, and provide insights for long-term strategies for reconciling urban environment and economic development.

¹State Key Laboratory of Pollution Control and Resource Reuse and School of Environment, Nanjing University, Nanjing, China. ²School of Environment and Spatial Informatics, China University of Mining and Technology, Xuzhou, China. ³Laboratory for Climate and Ocean-Atmosphere Studies, Department of Atmospheric and Oceanic Sciences, School of Physics, Peking University, Beijing, China. ⁴Shenzhen Key Laboratory of Ecological Remediation and Carbon Sequestration, Institute of Environment and Ecology, Tsinghua Shenzhen International Graduate School, Tsinghua University, Shenzhen, China. ⁵State Environmental Protection Key Laboratory of Sources and Control of Air Pollution Complex, Beijing, China. ⁶Jiangsu Collaborative Innovation Center of Atmospheric Environment and Equipment Technology (CICAET), Nanjing University of Information Science and Technology, Nanjing, China.

✉e-mail: yuzhao@nju.edu.cn

Table 1 | The 11 major events and their main emission control periods, event duration and the inversion simulation period of NO_x emissions

Event name	Abbreviation	Host city	Main control period	Event duration	Inversion simulation period
2010 Expo China	2010 EXPO	Shanghai	1 Apr.–31 Oct. 2010	1 May–31 Oct. 2010	1 Mar.–30 Nov. 2010
2013 Asian Youth Games	2013 AYG	Nanjing	1–31 Aug. 2013	16–24 Aug. 2013	1 July–30 Sept. 2013
2014 Youth Olympic Games	2014 YOG	Nanjing	15 July–31 Aug. 2014	16–28 Aug. 2014	1 July–30 Sept. 2014
2014 National Memorial Day	2014 NMD	Nanjing	17 Nov.–17 Dec. 2014	13 Dec. 2014	1 Nov.–31 Dec. 2014
2015 National Memorial Day	2015 NMD	Nanjing	7–15 Dec. 2015	13 Dec. 2015	1 Nov.–31 Dec. 2015
2016 G20 Summit	2016 G20	Hangzhou	1 Aug.–6 Sept. 2016	4–5 Sept. 2016	1 July–31 Sept. 2016
2016 National Memorial Day	2016 NMD	Nanjing	9–13 Dec. 2016	13 Dec. 2016	1 Nov.–31 Dec. 2016
2018 International Import Expo China	2018 CIIE	Shanghai	27 Oct.–10 Nov. 2018	5–10 Nov. 2018	1 Oct.–31 Nov. 2018
2019 International Import Expo China	2019 CIIE	Shanghai	27 Oct.–10 Nov. 2019	5–10 Nov. 2019	1 Oct.–31 Nov. 2019
2020 International Import Expo China	2020 CIIE	Shanghai	1–10 Nov. 2020	5–10 Nov. 2020	1 Oct.–31 Nov. 2020
2023 19th Asian Games	2023 AG	Hangzhou	10 Sept.–8 Oct. 2023	23 Sept.–8 Oct. 2023	1 Aug.–31 Oct. 2023

A number of studies have evaluated the effectiveness of short-term measures on air quality at major events, in particular, those hosted in Beijing, the capital city of China^{10–12}. For example, enhanced emission controls were demonstrated to play a crucial role in air quality improvement during the 2008 Beijing Olympics. Daily emissions of nitrogen oxides (NO_x) during the event were estimated to be cut by 47% compared with the June 2008 level based on a ‘bottom-up’ investigation¹¹. Most existing studies focused on a single event, examining the variation in daily air quality or monthly emissions around the event period⁶. Due to a lack of information on instantly changing emissions, the impacts of meteorology and emission controls on air quality improvement for the host city have not been fully evaluated. More importantly, the similarities and differences in the short-term emissions reductions for multiple major events hosted in various cities, as well as their main drivers, remain poorly understood. Such research gaps prevent a full understanding of the changing effectiveness of short-term intensive controls, along with the continuous implementation of long-term national air quality policies, and largely weaken the scientific design of pollution controls with a comprehensive consideration of economic, social and environmental benefits.

The above limitations result mainly from inadequate data and knowledge of fast-changing emissions at a relatively fine temporal (for example, daily or weekly) and horizontal (for example, city or regional) resolution. Emission inventories developed with the ‘bottom-up’ approach, which relies on annual energy consumption and industrial production, failed to track the short-term changes in human activities¹³. ‘Top-down’ inversion, which uses satellite-derived tropospheric vertical column densities (TVCDs) as a constraint for emissions of specific air pollutants, such as nitrogen dioxide (NO₂), improves the capability of capturing the spatiotemporal pattern of emissions^{14–17}. However, there are substantial data gaps in daily TVCDs caused by cloud cover or instrumental deficiency¹⁸, and the horizontal resolutions of most satellite observations are too coarse for city-level evaluation (for example, the ground pixel size of 40 × 80 km² for Global Ozone Monitoring Experiment-2 (GOME-2)¹⁹ and an overall resolution of 13 × 24 km² at nadir for Ozone Measure Instrument (OMI)²⁰). Although the Tropospheric Monitoring Instrument (TROPOMI)²¹ has greatly improved the resolution to 3.5 × 7 km², the events before its launch (July 2018) could not benefit from its high-resolution observations unless specific data fusion took place.

In this study, we selected NO_x as the target species and investigated the changing emission abatement resulting from short-term emission controls for 11 major events (Table 1) hosted in different cities in the Yangtze River Delta (YRD) region of China from 2010 to 2023 (see Supplementary Fig. 1 for the locations and cities of the YRD). NO_x

is highly involved in the formation of fine particulate matter (PM_{2.5}) and ozone (O₃), and comes from both natural (for example, soil and lightning) and anthropogenic sources. In the YRD, with abundant anthropogenic activities, NO_x emissions are more closely associated with energy use and traffic. To summarize our approach, we first developed a novel strategy that combines available satellite observations and a machine learning algorithm to obtain a reconstructed dataset of NO₂ TVCDs (RETOMI2). In this dataset, the data gaps are greatly filled and the horizontal resolution for the YRD is improved. We then inferred 7-day moving averages of NO_x emissions at the city level around each of the 11 events (‘the a posteriori emissions’) using a top-down inversion that combines the Multiple-resolution Emission Inventory for China (MEIC)^{22,23}, RETOMI2 and air quality modeling using the Weather Research and Forecasting–Community Multi-scale Air Quality (WRF-CMAQ) model^{24,25} at a horizontal resolution of 9 × 9 km². We also analyzed and compared the maximum effectiveness of short-term emission controls across events, identified as the difference between the lowest daily NO_x emissions (expressed as the 7-day moving average) during the main control period and the 7-day average emissions before the period. Finally, we quantified the contributions of emission and meteorological variation to the observed changes in NO₂ concentration for each event to demonstrate the benefit of short-term controls on air quality.

Results

Improvement of the reconstructed NO₂ TVCD dataset (RETOMI2)

Figure 1 illustrates the enhanced quality of our reconstructed NO₂ TVCD dataset (RETOMI2) compared with the Peking University Ozone Monitoring Instrument NO₂ (POMINO) and POMINO-TROPOMI products developed by Peking University (<http://www.pku-atmos-acm.org/acm-Product.php/>). Derived respectively from OMI and TROPOMI measurements, POMINO and POMINO-TROPOMI take into account China’s aerosol optical effect on NO₂ retrieval and achieve more reasonable TVCDs for the country than global-level products^{21,26}. Briefly, we performed three main steps to create RETOMI2 with improved horizontal resolution and spatiotemporal coverage compared with POMINO: (1) we filled the data missing in POMINO with support from GOME-2, (2) we expanded the temporal coverage of POMINO-TROPOMI with support from step 1, and (3) we expanded the spatial coverage of step 2. The key procedures included the application of eXtreme Gradient Boosting (XGBoost) in steps 1 and 2, and the application of Data Interpolation Empirical Orthogonal Functions (DINEOF) in step 3. XGBoost was used to build the relationships between different satellite products and helped to obtain a long-term NO₂ TVCD record with a high horizontal

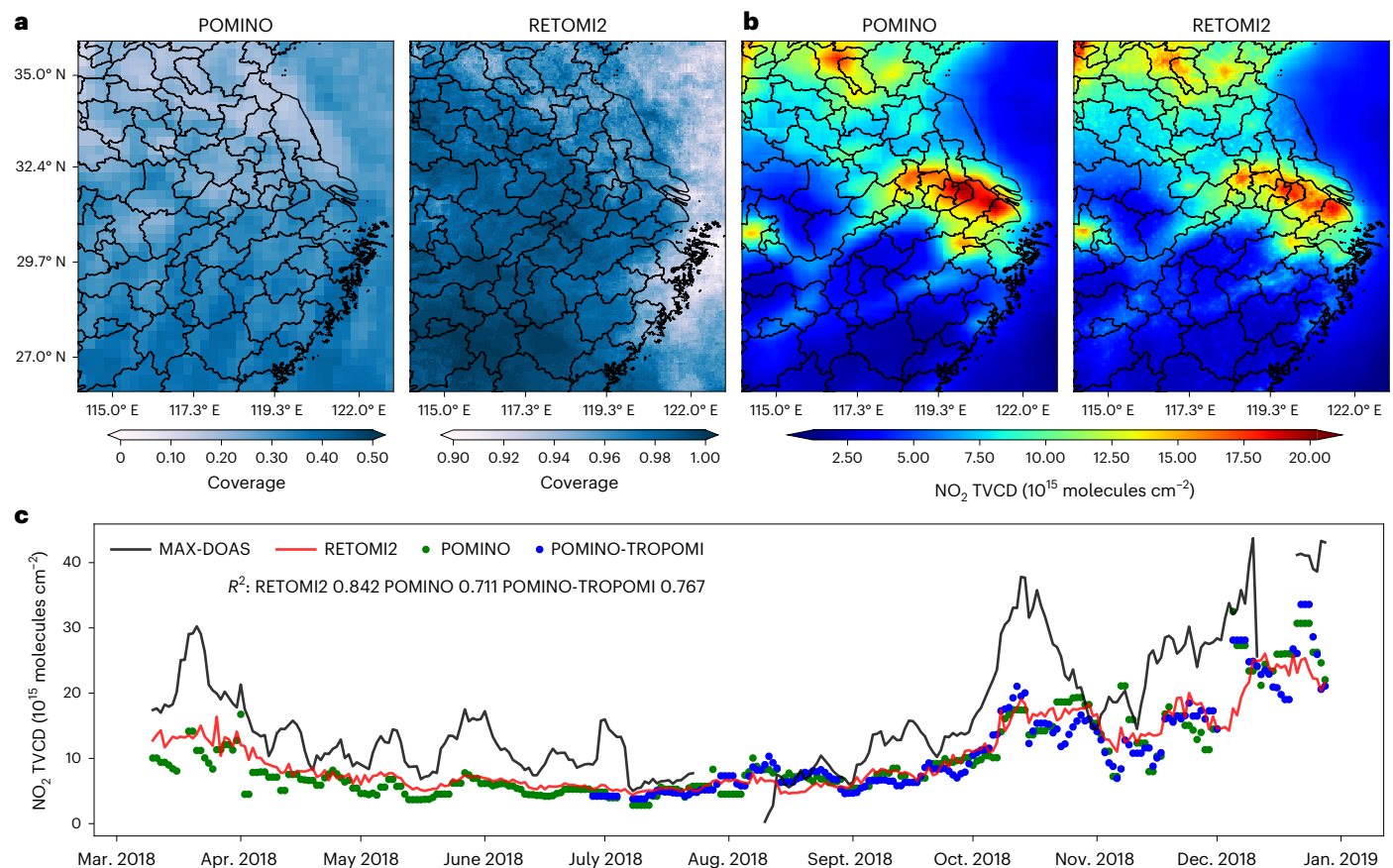


Fig. 1 | Improvements of RETOMI2 compared with POMINO, POMINO-TROPOMI and MAX-DOAS. **a, b**, Data coverage (**a**) and spatial patterns (**b**) of NO₂ TVCDs in POMINO and RETOMI2 for the main control periods of the 11 major events. The horizontal resolution is 0.25° × 0.25° for POMINO and 0.05° × 0.05° for RETOMI2. **c**, Time series of 7-day moving averages of NO₂ TVCDs derived from RETOMI2, MAX-DOAS and POMINO for Xuzhou (117.14° E, 34.22° N; for its

location, see Supplementary Fig. 2) from March to December 2018. The data from POMINO-TROPOMI are from June to December 2018. The map data were provided by the Resource and Environment Science and Data Center Institute of Geographic Sciences and Natural Resources Research, Chinese Academy of Sciences (<https://doi.org/10.12078/2023010103>, 2023)⁴⁸.

resolution (0.05° × 0.05°), while DINEOF further filled the data gap and helped to obtain RETOMI2 for the YRD.

As shown in Fig. 1, the RETOMI2 dataset has a clear advantage in spatial coverage, horizontal resolution and reliability in the daily variation of NO₂ TVCDs compared with the two domestic products. Specifically, RETOMI2 shows a 67% improved spatial coverage compared with POMINO for the YRD during the main control periods of the 11 events (Fig. 1a). A consistent spatial distribution was found between the two products with the correlation coefficient calculated at 0.96 (Fig. 1b). Compared with POMINO, with a coarser resolution (0.25° × 0.25°), RETOMI2 (0.05° × 0.05°) presents a more subtle regional variation of NO₂ TVCDs and thus can better capture hotspots and rapid changes in urban areas.

In addition, the standard deviation of RETOMI2 is smaller than that of POMINO for most of the YRD, with the average difference estimated at -24.1% for the whole region (Supplementary Fig. 3). Figure 1c shows the daily NO₂ TVCDs from satellite retrievals and multi-axis differential optical absorption spectroscopy (MAX-DOAS) measurements for 2018 at a single site, Xuzhou, in the YRD (depending on the availability of observations; see Supplementary Fig. 4 for monthly TVCDs from 2014 to 2016 at various sites). In general, satellite-derived TVCDs are consistently lower than those from MAX-DOAS, which is attributed to the various retrieval techniques used and the effect of cloud cover on satellite measurements²⁶. Among the satellite-derived products, RETOMI2 agrees best with the MAX-DOAS observations, with the highest correlation coefficients during the comparison periods for

different cities. The comparisons demonstrate that RETOMI2 improves the estimation of the spatiotemporal pattern of NO₂ TVCDs and thus is suitable for evaluating the changing NO_x emissions at the city level.

The a posteriori NO_x emissions for the events in host cities

Combined with RETOMI2 constraints, the a posteriori daily emissions were demonstrated to better track the short-term variation in NO_x emissions at the city level. The a posteriori emissions of NO_x were 6–29% lower than those of MEIC, the current best available emissions data from the ‘bottom-up’ approach, for the main control periods of all the concerned events in the YRD (Supplementary Table 1). The a posteriori emissions also better support the NO₂, PM_{2.5} and O₃ concentration simulations for the main control periods of all the concerned events in the YRD (Supplementary Tables 2–4). Specifically, the correlation coefficients (*R*) between simulations and observations were elevated by about 0.02–0.1, 0.01–0.29 and 0.01–0.41 for NO₂, PM_{2.5} and O₃, respectively. The normalized mean bias (NMB) and normalized mean error (NME) were reduced from 50% to -4% and 51% to 23% for NO₂, from 15% to 13% and 40% to 34% for PM_{2.5}, and from -22% to 18% and 33% to 32% for O₃, respectively. Note that the reductions in NO_x emissions during the concerned periods always enhanced O₃ concentrations, which is attributed to a prevailing ‘volatile organic compound-limited’ O₃ formation regime in the YRD, under which O₃ is more sensitive to volatile organic compounds and can be removed by ‘titration reaction’ with NO (refs. 27–29).

Figure 2 presents the 7-day moving averages of the a posteriori emissions of the host cities Shanghai, Nanjing and Hangzhou around

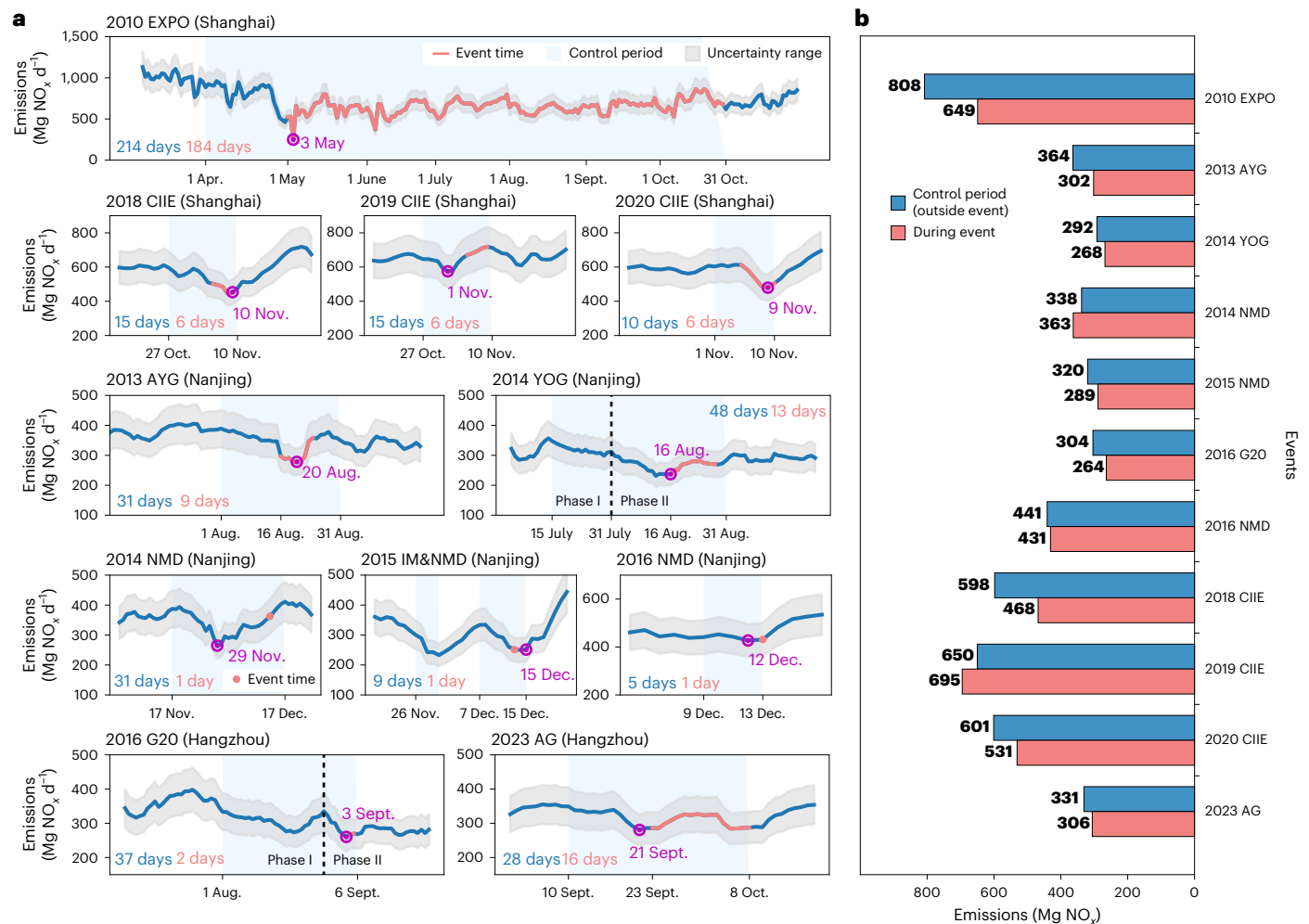


Fig. 2 | Seven-day moving averages of the total NO_x emissions for the three host cities during the 11 major events. a, The 7-day moving averages of NO_x emissions with the random error (expressed as 95% confidence interval) indicated by gray shading. The blue shading shows the main control period and the red curves represent the event period (note dots are used for the 1-day events of 2014–2016 NMD). The corresponding durations are shown in blue and red, respectively. The purple circles indicate the day on which the trend in NO_x emissions reversed from decline to growth. The black dashed vertical lines for 2014 YOG and 2016

G20 separate different control phases (phase I and phase II). Note that the 2015 International Marathon (2015 IM), hosted from 26 to 29 November 2015 in Nanjing, adopted the same temporary emission regulations as 2015 NMD, leading to declining emissions during the event period. We illustrate the emissions data of 2015 IM in the figure, but did not include it in the analysis in this study. **b**, Daily average NO_x emissions for the event period and the control period outside of the event for all 11 events.

individual major events. Emissions were clearly reduced during the control periods of most events (blue shading in Fig. 2a), and rebounds were also observed for most events. The purple circles in the graphs indicate the points at which the emissions reversed from decline to growth. For 2010 World Expo (2010 EXPO), 2013 Asian Youth Games (2013 AYG), 2014 Youth Olympic Games (2014 YOG), 2014, 2015 and 2016 National Memorial Day (2014 NMD, 2015 NMD and 2016 NMD, respectively), 2016 Group of Twenty Summit (2016 G20), 2018, 2019 and 2020 International Import Expo China (2018 CIIE, 2019 CIIE and 2020 CIIE, respectively), and 2023 19th Asian Games (2023 AG), the daily NO_x emissions were estimated to decline by 630, 110, 120, 190, 120, 60, 10, 250, 100, 390 and 60 Mg, respectively, from the start of the control periods to the reversal point. These results confirm that short-term emission controls were effective in limiting NO_x emissions during events.

Shanghai and Nanjing held their first global events (2010 EXPO and 2013 AYG, respectively) in the early 2010s. Due to the lack of experience in short-term air quality improvement, many more stringent temporal measures than usual were imposed before the events, leading to relatively large emission abatement. However, the emissions rebounded

shortly after these events started (about 4 days later). In contrast, the controls of subsequent events presented a gradual and consistent decline in emissions, implying more sustainable emission control practices. Two series of events, NMD and CIIE, have been organized annually since 2014 in Nanjing and since 2018 in Shanghai, respectively. The lengths of the control periods for the NMD and CIIE events were shortened year by year (31, 9 and 5 days for NMD from 2014 to 2016, and 15, 15 and 10 days for CIIE from 2018 to 2020). The shortened control periods reflect a more cautious strategy, aiming at minimizing the disruption to regular economic activities and daily lives.

The big changes (declines and rebounds) observed in NO_x emissions during the main control period typically correspond to the timeline (beginning and end) of the short-term intensified measures. The staged implementation of control measures led to progressive abatement of emissions (see Supplementary Table 5 for details of the intensified measures). During 2014 YOG, for example, control measures were implemented in two phases (phase I, 15–31 July and phase II, 1–31 August). Phase II provided stricter controls on point, area and mobile sources. Consequently, the NO_x emissions began to decline from 15 July, followed by a more substantial reduction from 1 August.

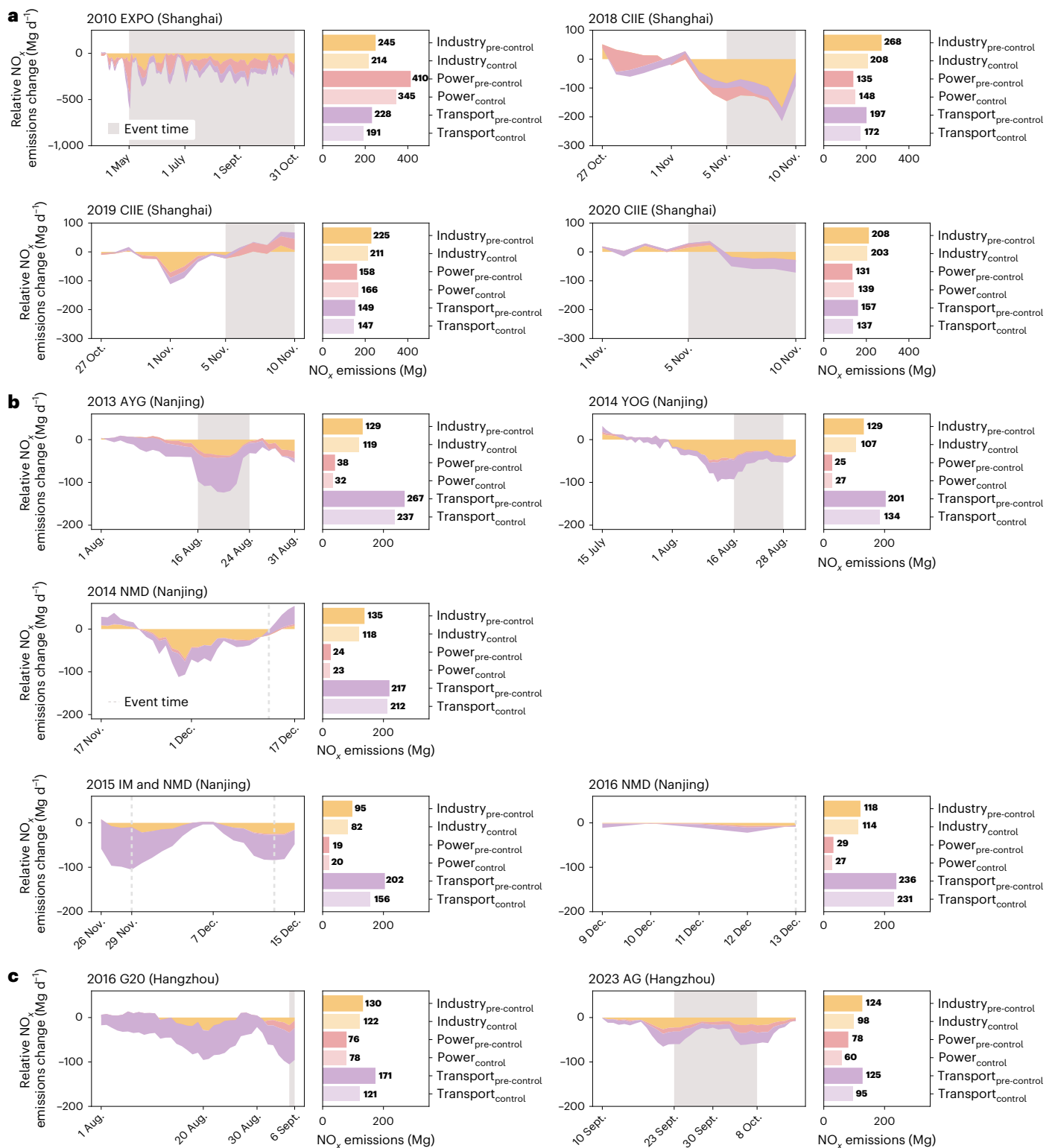


Fig. 3 | Decomposition of the changing NO_x emissions for the host cities during the main control periods by sector. a–c. Sector-level changes in NO_x emissions are shown for the major events hosted in Shanghai (a), Nanjing (b) and Hangzhou (c). The 7-day averages of NO_x emissions immediately before the control period

are represented as Industry_{pre-control}, Power_{pre-control} and Transport_{pre-control}, and those during the control period are Industry_{control}, Power_{control} and Transport_{control}. The gray shading and dotted vertical lines represent the event time.

The rates of emissions decline were estimated at 6.6 and 6.9 Mg d⁻¹ for the two phases, respectively. Similarly, during phase II of 2016 G20 (28 August–3 September), the government adopted additional control measures for mobile sources and emergency control measures compared with phase I (1–27 August), which resulted in a big reduction in

NO_x emissions from 28 August (the rates of decline for the two phases were 6.2 and 10.9 Mg d⁻¹, respectively). In general, the average daily NO_x emissions were at their lowest during the event period (within and shorter than the main control period) for most major events as this was usually the period with the most stringent short-term controls (Fig. 2b).

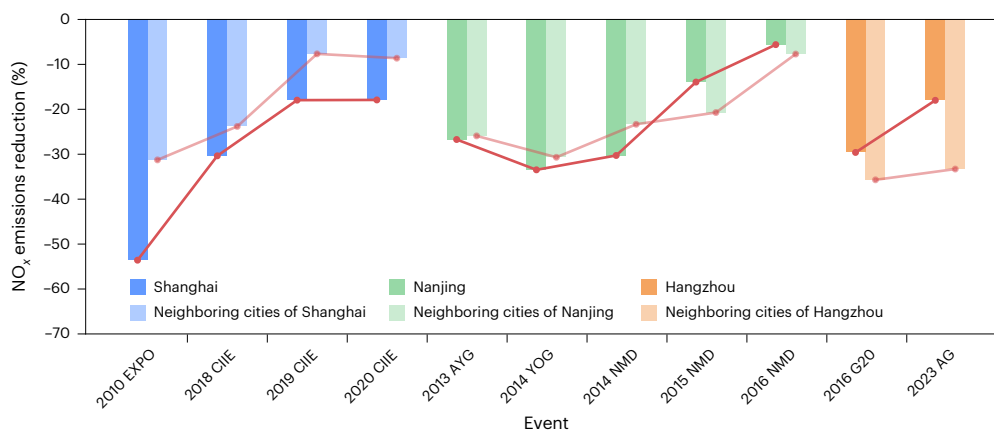


Fig. 4 | Effectiveness of short-term controls in the host and neighboring cities for major events. Relative changes in NO_x emissions in Shanghai, Nanjing and Hangzhou and their neighboring cities during the main control periods of individual events. The lines highlight the gradually reduced benefit of short-term controls on emission abatement for individual regions.

Drivers of emission change during major events

Figure 3 shows the NO_x emissions by sector around the 11 major events. The 7-day averages immediately before the main control period and those during the period were compared to assess the relative changes in emissions. Shanghai is one of the most industrialized cities in China, with the annual NO_x emissions reaching 431 Gg in 2020 (data source: MEIC). The power sector was identified as the main driver of the change in NO_x emissions during 2010 EXPO (Fig. 3a). Compared to the pre-control period, the NO_x emissions from the power sector declined by 15.9% for the main control period, accounting for 49% of the total reduction in NO_x emissions during this period. The large reduction in power sector emissions was mainly a result of the enhanced use of selective catalyst reduction (SCR) systems. Industry and transport played a greater role in reducing emissions during 2018, 2019 and 2020 CIIE, accounting for 71%, 87% and 80% of the total reduction, respectively. This shift in the main sectors responsible for the short-term emissions reductions reflects the diverse progress of the emission controls for different sectors. The power sector was a major contributor of NO_x emissions in the early 2010s³⁰. After 2010 EXPO, Shanghai continued to improve SCR penetration and operation as part of its regular air quality measures, and consequently the NO_x emissions from the power sector in the city have shown a prominent downward trend since 2010, stabilizing during 2016–2020 with an abatement of approximately 65% compared to the 2010 level (MEIC; Supplementary Fig. 5b,f). Improved regular controls have largely reduced the extra benefit of short-term measures on power plants during the major events. Therefore, the measures for later events focused more on the industry and transport sectors (Supplementary Table 5).

Nanjing, the capital of Jiangsu Province, is also highly industrialized, with the annual level of NO_x emissions around half that of Shanghai. The main driver of emission changes in 2014 was the industry sector, accounting for 59% and 74% of the total reduction for 2014 YOG and 2014 NMD, respectively (Fig. 3b). Transport was more important for other events, accounting for 65%, 77% and 45% of the total reduction for 2013 AVG, 2015 NMD and 2016 NMD, respectively. As a legacy of 2014 YOG, in particular, the Nanjing government has continuously implemented stringent emission controls on industrial sources as part of its regular actions, such as the closure of all small coal-fired boilers. As a result, the industry sector was not the major driver of emissions reduction for subsequent events, with a gradually weakening benefit from short-term measures (reductions of 22, 17, 13 and 4 Mg d⁻¹ for 2014 YOG, 2014 NMD, 2015 NMD and 2016 NMD, respectively). Hangzhou is a developed city dominated by the tertiary sector. Transport was the main sector driver of emission abatement for 2016 G20 and 2023 AG,

accounting for 89% and 41% of the total reduction during the main control periods, respectively (Fig. 3c).

Reducing the benefit of short-term controls for events

Figure 4 illustrates the effectiveness of short-term controls (or maximum daily emissions reduction, expressed as the relative difference between the smallest daily NO_x emissions during the main control period (7-day moving average) and the 7-day average before this period) in the host and neighboring cities for the major events. For the events hosted in Shanghai, the effectiveness declined from 2010 to 2020. The maximum daily emissions reduction in Shanghai decreased from 53.6% for 2010 EXPO to 17.9% for 2020 CIIE, while the reduction in neighboring cities decreased from 31.3% for 2010 EXPO to 7.7% for 2019 CIIE, followed by a slight increase to 8.6% for 2020 CIIE. The effectiveness (or marginal benefit) of short-term measures was greater for Shanghai than for neighboring cities for all four events. This implies a more comprehensive design and more exhaustive implementation of the temporary measures in Shanghai, for example, better planning of city transport to reduce traffic congestion and stricter supervision of industrial plants to ensure the full operation of air pollutant control devices.

For the events hosted in Nanjing, the effectiveness of emission controls grew from 2013 to 2014, but then declined from 2014 to 2016. The maximum daily reductions for Nanjing were estimated at 26.7%, 33.5%, 30.3%, 13.9% and 5.6% for 2013 AVG, 2013 YOG, 2014 NMD, 2015 NMD and 2016 NMD, respectively, while the analogous numbers were 25.9%, 30.7%, 23.3%, 20.7% and 7.7% for neighboring cities, respectively. For the events hosted in Hangzhou, the maximum daily reduction in NO_x emissions declined from 29.6% for 2016 G20 to 18.0% for 2023 AG for Hangzhou, and from 35.7% to 33.3% for neighboring cities. Since 2015, the short-term controls in the host cities Nanjing and Hangzhou have been less effective in reducing emissions than in the neighboring cities, in contrast to the events held in Shanghai. This is partly a result of the faster progress and/or greater abundance of regular emission controls in Nanjing and Hangzhou than in their neighboring cities³¹, which might partly mask the extra effect of short-term controls specifically for the events.

Among different events, the maximum daily reduction in NO_x emissions ranged between 5.6% and 54.0%. A clear downward trend existed in the overall opportunity of short-term measures on extra emission abatement in the host and neighboring cities over the period of 2010–2023, which was associated with the increasingly conservative implementation of temporal emission controls for events, as previously mentioned. Moreover, the improving implementation of long-term air quality policies has reduced NO_x emissions, thereby limiting the marginal benefit of short-term measures on emissions reduction. Long-term policies, such as the implementation of gradually tightened

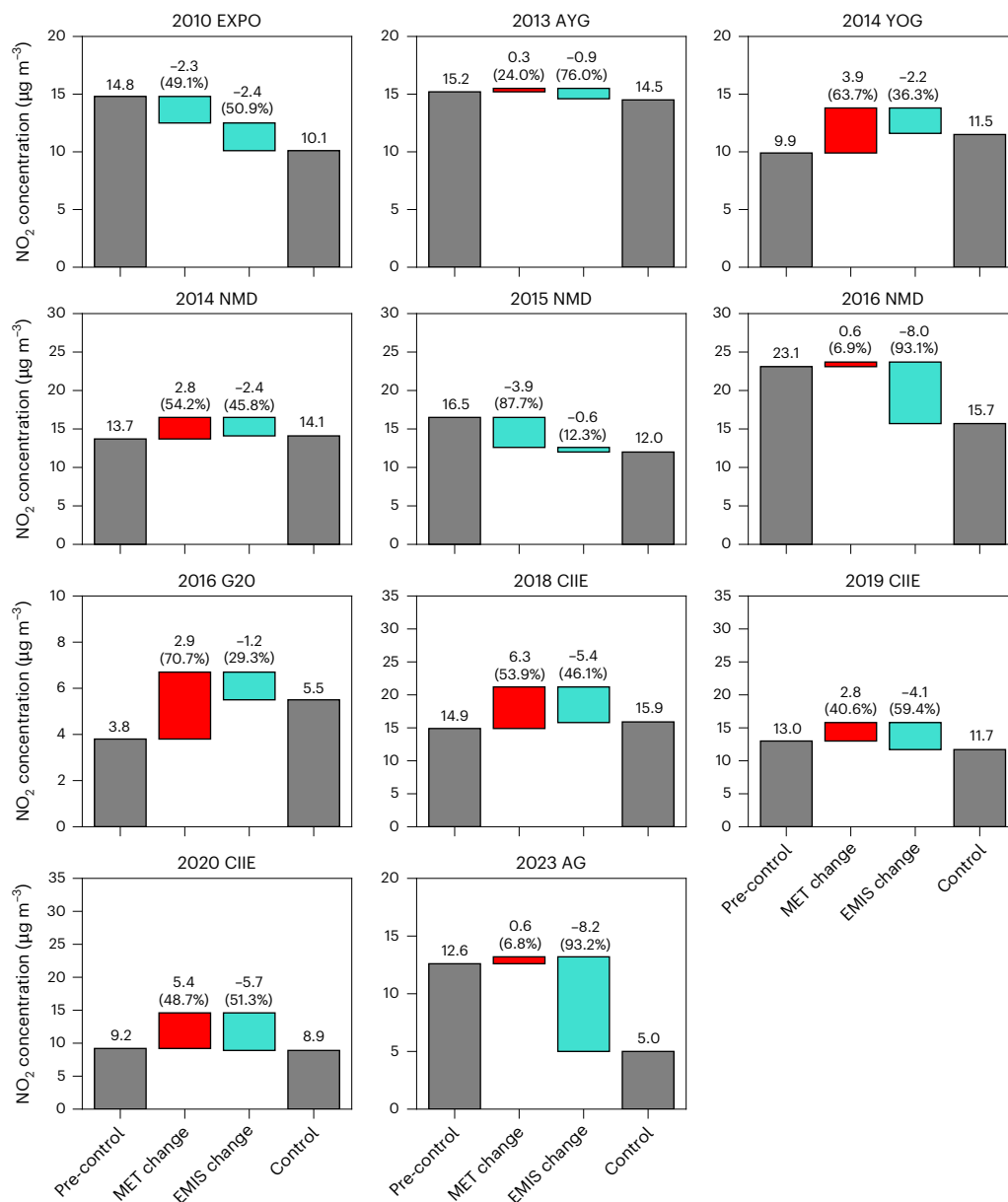


Fig. 5 | Effect of meteorology and emission variation on NO_2 concentrations. Contribution of meteorology and emission variation to the changing NO_2 concentrations for the host cities from the pre-control period (P1) to the control period (P2) of different events. P2 is essentially equivalent to the main control period of the major events, except for 2010 EXPO (Supplementary Table 6), and

P1 is the time period before P2 with the same duration as P2. The two gray bars in each plot show the simulated average NO_2 concentrations for P1 and P2. The two central bars represent the contribution of meteorology (MET) and emissions (EMIS), with the red and cyan indicating an increase and decrease in the NO_2 concentration, respectively.

emissions standards, increasing the use of end-of-pipe emission control devices, and the retirement of small and inefficient factories, have greatly reduced the so-called super emitters. Consequently, the extra benefit of the temporary closure of super emitters for individual events has greatly shrink.

Impacts of emissions and meteorology on NO_2 concentration

The change in NO_2 concentration from the pre-control to the control period (see Supplementary Table 6 for definitions) was decomposed into meteorological- and emission-induced contributions for each of the 11 events (Fig. 5; see Methods for details of the simulation experiments). Compared to the pre-control period, the NO_2 concentrations were estimated to decline during the main control period by 31.8%, 4.6%, 27.3%, 32.0%, 10.0%, 3.3% and 60.3% for 2010 EXPO, 2013AYG, 2015 NMD, 2016 NMD, 2019 CIIE, 2020 CIIE and 2023 AG, respectively, while

they were estimated to increase by 16.2%, 2.9%, 44.7% and 6.7% for 2014 YOG, 2014 NMD, 2016 G20 and 2018 CIIE, respectively.

For most events (except 2010 EXPO and 2015 NMD), meteorological variation enhanced NO_2 concentration, while emission controls more or less offset it. In particular, meteorological variation contributed 63.7% and 70.7% to the rise in NO_2 concentration for the host cities in 2014 YOG (Nanjing) and 2016 G20 (Hangzhou), respectively. Measurements revealed that the NO_2 concentration during 2014 YOG (16–28 August) did not present a clear decline, as it did during 2013 AYG in Nanjing (Supplementary Fig. 6), while short-term controls resulted in a greater reduction in NO_2 concentration for 2014 YOG ($-2.2 \mu\text{g m}^{-3}$) than for 2013 AYG ($-0.9 \mu\text{g m}^{-3}$). A less favorable diffusion condition was thus indicated for 2014 YOG than for 2013 AYG. Lower wind speed and lower planetary boundary layer height weakened the dispersion of atmospheric pollutants, while lower 2-m temperatures reduced convective

instability (Supplementary Fig. 7). For 2016 G20, there was a decline in 10-m wind speed over Hangzhou in phase II (28 August–6 September), which facilitated pollutant formation and accumulation in the city. The decline in the planetary boundary layer height and surface temperature also affected the diffusion of pollutants. However, during 4–5 September, the concentration of pollutants, in particular, particulate matter, did not increase, which is attributed to the large emissions reduction (Supplementary Fig. 8). Therefore, the short-term controls greatly overcame the adverse impact of meteorology and improved air quality for the event.

Discussion

Using a reconstructed database of NO₂ TVCDs as constraints and an inverse modeling system, we have presented here the estimates of 7-day moving averages of NO_x emissions for 11 major events hosted in east China. The results support analyzing the effectiveness of short-term emission controls in developed cities in China. Moreover, combined with existing long-term air pollution regulations, the outcomes shed light on future strategy design and policy-making for national air quality improvement.

Our findings confirmed the crucial role of short-term measures in reducing NO_x emission during the 11 major events. However, the opportunity of temporal measures to provide extra emission abatement has gradually declined, mainly due to the continuous implementation of tightened long-term air quality policies. Moreover, for short-term controls in cities, there has been a shift from the implementation of extremely stringent and extensive measures to a more conservative strategy with limited but precise actions on key emitters, aiming to minimize disruption to regular daily lives. Temporal measures might be more effective in neighboring cities than in the host cities of the events as the more stringent regular controls for the latter have reduced the potential for further emission abatement for events. The transition of the major driver of emissions reduction from power to the industry and transport sectors reflects the successful efforts to reduce emissions from power plants over the long term, including compulsory retrofitting with ultralow emission technologies. Moreover, after events, specific useful short-term measures on air quality improvement would be adapted and incorporated into long-term air quality policies. These included strict supervision and monitoring of targeted sectors with greater emission abatement potential and better cooperation of pollution controls across different regions. Enhanced regular air quality policies commonly appeared immediately after individual major events in the YRD (Supplementary Fig. 9). Therefore, measures initiated for short-term events not only resulted in immediate environmental benefits, but also supported long-term air quality improvement.

Unfavorable meteorological conditions remained one of the main factors contributing to heavy urban pollution during major events. It is thus crucial to improve air quality forecasting and warning before major events to mitigate the impact. Accurate prediction of short-term meteorological conditions and air quality in advance can provide strong technical support for the government to conduct timely supervision and control of air pollution sources, overcoming the effect of unfavorable weather conditions. More comprehensive online measurements of economic activity and pollution sources are thus recommended to obtain near-real-time emissions data, which can consequently improve the capability of air quality forecasting. Moreover, with the background of climate change, efforts should be continuously made to maintain the downward trend in air pollutant emissions and to prevent worsening air quality resulting from possible oscillating meteorology.

The uncertainties in this work lie in the satellite observations of NO₂ TVCDs¹⁹, insufficient consideration of regional transport in the emission inversion and the decomposition of NO_x emissions into individual sectors. Satellite measurements are generally less sensitive to near-surface concentrations than MAX-DOAS, leading to the underestimation of NO₂ TVCDs (Fig. 1). To reduce such uncertainty, we improved and applied averaging kernels (AK), which indicate the sensitivities of

satellite measurements at different vertical levels in the a posteriori emission estimation (see Methods for details). Moreover, the underestimation of NO₂ TVCDs was recognized as a systematic bias that barely influences temporal variability, thus it would not change the main findings of this work. In addition to anthropogenic sources, natural sources (for example, lightning) contribute to TVCDs. Following Kong et al.³², who assumed that the background TVCD, including the contribution from lightning, was half the minimum observed NO₂ TVCD, we selected 2014 YOG as an example and recalculated the a posteriori emissions. A small difference from the original estimate was found, with NMB and NME values of −0.2% and 7%, respectively. To examine the bias in NO_x emission inversion due to regional transport, we performed a sensitivity simulation at a coarser horizontal resolution of 27 × 27 km². The results showed that the difference in resolution barely affected urban-scale inversion in this study (Supplementary Text 1 and Supplementary Table 7). The uncertainty in the estimation of sector-level emissions was also investigated by changing the criterion for defining the main emission sectors of individual grid cells within the simulation domain (Supplementary Fig. 2), with a small difference found for the inversed sector-level emissions (Methods, Supplementary Text 1 and Supplementary Table 8). In the future, further improvement in the estimation of short-term emissions at the city level could be achieved by incorporating more advanced artificial intelligence and air quality simulation technologies, as well as by measurement of TVCDs at high temporal resolution with geostationary satellites.

Methods

Integrated model framework

The methodological framework for this work is shown in Supplementary Fig. 10. It consists of four main modules (A–D). First, we reconstructed the satellite-derived NO₂ TVCDs (RETOMI2) dataset by filling in missing data and improving the resolution with XGBoost and DINEOF. Python v3.9 and Matlab v9.13.0 (R2022b) were used to conduct XGBoost and DINEOF, respectively. We then developed an inverse modeling system based on RETOMI2 and a coupled WRF-CMAQ model. The system integrates a mass balance method and relative error weighting with bottom-up estimates (MEIC) to deduce the 7-day moving averages of total NO_x emissions (the a posteriori emissions) around individual major events. Next, we combined the a posteriori emissions and bottom-up estimates to constrain the NO_x emissions by sector and then decomposed the difference in NO_x emissions between the main control period and the week before the control period into individual sectors. Last, the a posteriori emissions were applied in WRF-CMAQ to separate the contributions of meteorological and emission variations to the changing NO₂ concentrations for the host cities during major events.

Data source

The primary NO₂ TVCD data were obtained from three satellite products: OMI on board Aura (2004–present) with an equator crossing time of 13:45 local time, GOME-2 on MetOp-B (2012–present) with an equator crossing time of around 09:30 local time and TROPOMI on the Copernicus Sentinel-5 Precursor satellite with an equator crossing time of 13:30 local time. We developed a machine learning approach by year to estimate the NO₂ TVCDs for 2010–2020 and 2023 for the YRD (2011, 2012 and 2017 were excluded as there were no major events in those years). Only pixels with a view zenith angle less than 30°, cloud radiation fraction less than 50% and aerosol optical depth less than 3 were used for the analysis. Moreover, the AKs from the level 2 products of POMINO and POMINO-TROPOMI were also processed and then applied in the subsequent comparison of the observations with simulations, taking into account the sensitivity of satellite measurements to different altitudes in the atmosphere^{33–35}.

In total, 38 variables were selected as model predictors for XGBoost (Supplementary Tables 9–11), including meteorological factors, land use factors, social and economic conditions, and

spatiotemporal information. AK-related parameters such as the solar zenith angle and observation angle were also included. Meteorological variables were downloaded from the ERA5 hourly atmospheric reanalysis dataset (accessible online through <https://cds.climate.copernicus.eu/datasets/>). Land use data were extracted from the Finer Resolution Observation and Monitoring of Global Land Cover (FROM-GLC 2017v1) dataset (accessible online through <https://data-starcloud.pcl.ac.cn/iearthdata/>), which contains nine land use types at a spatial resolution of $30 \times 30 \text{ m}^2$ (ref. 36). Four types of land use (cropland, impervious surface, forest and water surface) were selected as they occupy over 87% of the YRD territory. Population density data were obtained from WordPop (<https://hub.worldpop.org/geodata/summary?id=44833>).

We used MAX-DOAS measurements at four sites to evaluate the performance of the reconstructed data. Monthly data (within January 2014–January 2017) were available for three sites in Hefei, Nanjing and Shanghai³⁷ and daily data (March 2018–January 2019) were available for Xuzhou³⁸. For the daily data, we averaged all valid MAX-DOAS measurements within $\pm 1 \text{ h}$ of the TROPOMI overpass time and compared them with the satellite-derived data for the single grid cell where the site was located. The bottom-up estimates of NO_x emissions were taken from MEIC (<http://www.meicmodel.org>). Biogenic emissions were provided by the Model of Emissions of Gases and Aerosols from Nature (MEGAN v3.1, <https://bai.ess.uci.edu/megan>). As shown in Supplementary Fig. 11, soil NO_x contributed 1.3–4.4% of the total NO_x emissions for the five events conducted in summer and autumn, and less than 1% for the other six events in winter. Ground observations of meteorological variables at 3-h intervals were downloaded from the National Climatic Data Center to evaluate the WRF modeling performance (2010–2023). Daily surface concentrations of air pollutants for 2014–2023 in the YRD were observed at state-operated air quality monitoring stations and obtained from the Ministry of Ecology and Environment (<https://air.cnemc.cn:18007/>). A total of 567 observation stations were included to assess the model performance. NO_2 and O_3 concentrations were reported for the reference state (298.15 K and 1,013.25 hPa), and $\text{PM}_{2.5}$ concentrations at the actual monitoring conditions. We compared the original observation data with simulations, and the periods and/or stations with missing observation values due to equipment maintenance or power outages were excluded from model performance evaluation. The locations of the meteorological, air quality monitoring and MAX-DOAS stations are shown in Supplementary Fig. 2.

Predicting NO_2 TVCDs with an improved machine learning approach

XGBoost, a gradient boosting tree machine learning algorithm, was used in satellite data reconstruction, as shown in steps 1 and 2 in Supplementary Fig. 10a. For step 1, POMINO (as the target variable), GOME-2 and ancillary data (mainly meteorological reanalysis data, land use (with the original horizontal resolution of 30 m) and population density data ($1 \times 1 \text{ km}^2$)) were incorporated into XGBoost to obtain the reconstructed OMI product (REOMI), which expands the spatial coverage of POMINO to that of the union of POMINO and GOME-2. For step 2, POMINO-TROPOMI (as the new target variable), REOMI and ancillary data were incorporated to generate the reconstructed TROPOMI product (RETOMI), aiming to improve the resolution of REOMI. NO_2 data from POMINO, GOME-2, POMINO-TROPOMI and ancillary data (summarized in Supplementary Tables 9 and 10) were downsampled to the same horizontal resolution by bilinear interpolation ($0.25^\circ \times 0.25^\circ$ and $0.05^\circ \times 0.05^\circ$ for predicting REOMI and RETOMI, respectively). In addition to TVCDs, the AKs of the POMINO-TROPOMI (as the new target variable) and POMINO products and relevant satellite parameters were incorporated to create reconstructed AKs (REAK) via a similar process to step 2. Due to the lack of a POMINO dataset in 2023, we corrected the TVCDs (and AKs) using POMINO-TROPOMI for 2023 based on the correlation between the TVCDs (and AKs) of POMINO-TROPOMI and RETOMI from 2018 to 2020 (Supplementary Figs. 12 and 13).

Tenfold cross-validation was performed to evaluate the performance of the model for predicting REOMI, RETOMI and REAK. For each fold, the available data for each model were divided into a training set (90%) and a validation set (10%). As shown in Supplementary Figs. 14–16, a satisfactory capability of model prediction was demonstrated by a small root mean squared error (RMSE) and mean average error and large coefficient of determination.

Filling the data gap with an optimized empirical orthogonal function method

We derived RETOMI2 (RETOMI with further data filled) products using the DINEOF method (step 3 in Supplementary Fig. 10a). The DINEOF was developed by Geo-Hydrodynamics and Environmental Research group at the University of Liège, Belgium, as a method for modeling the behavior of a numerical model without a priori information (by obtaining the necessary parameters on its own). In this method, empirical orthogonal functions (EOFs) were combined with interpolation techniques to reconstruct missing data caused by cloud cover, sensor limitations or other factors^{39,40}. The specific methods are described below.

First, in each selected year, RETOMI was processed as a matrix X ($m \times n$), where m and n are the spatial and temporal dimensions of the observation X , respectively. Meanwhile, 1% of the valid data in X were randomly selected as the cross-validation dataset X^c and then set to 0. The spatiotemporal mean of X was removed to highlight the pattern of variability. All missing points were set to 0. The initial number of modes P for EOF was set to 1 as the starting point for iterative analysis.

We then performed singular value decomposition of matrix X :

$$X = USV^T \quad (1)$$

where U ($m \times m$), S ($m \times n$), and V^T ($n \times n$) represent the spatial eigenmode, the singular value matrix and the transpose of the temporal eigenmode, respectively. Hence, the dataset of missing points X^{te} could be decomposed using equation (2):

$$X_{r,l}^{re} = \sum_{n=1}^P a_n(u_n)_r(v_n^T)_l \quad (2)$$

where r and l denote the rows and columns of the matrix X , respectively, a_n is the corresponding singular value, and u_n and v_n^T are the n columns of the spatial and transposed temporal eigenmodes, respectively. The RMSE of the cross-validation after reconstruction can be obtained with equation (3):

$$\text{RMSE} = \sqrt{\frac{1}{N} \sum_{n=1}^N (x_n^{re} - x_n^c)^2} \quad (3)$$

where N is the number of data points in the cross-validation set X^c , x_n^{re} denotes the reconstructed value at the n th data point, and x_n^c denotes the original observed value in the cross-validation set at the n th point. After completing the data for the missing points, the value of X^{te} can be expressed according to equation (4):

$$X^{re} = X + \partial X \quad (4)$$

where ∂X is the matrix of correction values for the missing points.

Next, we repeatedly applied equations (1)–(3) to the singular value decomposition of a new X^{te} until the RMSE converged (convergence level: 0.0001). Meanwhile, the maximum number of iterations to prevent the continuous non-convergence and the waste of computational cost was set to 300. The P value was incremented stepwise and the corresponding RMSE was recorded. A change in RMSE of less than 1% was considered satisfactory for this study (Supplementary Fig. 17). The corresponding P was set to P_b and the final reconstruction matrix X was obtained. Finally, X was added to the spatiotemporal mean derived

at the very beginning and inversely log-transformed to obtain the final reconstructed product RETOMI2.

Estimating a posteriori NO_x emissions with an inverse modeling system

We applied a mass balance method to obtain the ‘top-down’ estimates of the 7-day moving averages of NO_x emissions around individual major events in the YRD based on the difference between the simulated and observed NO₂ TVCDs and the relationship between the changing NO_x emissions and NO₂ TVCDs:

$$E_{t,i,\text{top-down}} = E_{t,i,\text{bottom-up}} \left(1 + \left(\frac{\Omega_{\text{obs}} - \Omega_{\text{sim}}}{\Omega_{\text{sim}}} \right)_{t,i} \beta_{t,i} \right) \quad (5)$$

where *i* represents a model grid cell (9 × 9 km²), *t* represents a 7-day time window, *E*_{*t,i*,top-down} is the ‘top-down’ estimation of NO_x emissions around an individual major event, *E*_{*t,i*,bottom-up} is the NO_x emissions from MEIC for the same period, *Ω*_{obs} represents the NO₂ TVCDs from RETOMI2, *Ω*_{sim} represents the simulated NO₂ TVCDs obtained with CMAQ and *β*_{*t,i*} is a unitless factor that represents the local sensitivity of NO₂ TVCDs to changing NO_x emissions.

A nested simulation using CMAQ v5.2 was conducted with the horizontal resolutions at 27 × 27 km² and 9 × 9 km² for domains 1 and 2, respectively (Supplementary Fig. 2). The meteorology field was driven by WRF v3.9.1. Details of the model settings have been described previously⁴¹. *β*_{*t,i*} was calculated as a comparison between a baseline simulation and an extra simulation with 10% perturbation in NO_x emissions (the emission perturbation level had a limited effect on *β*, Supplementary Text 1 and Supplementary Table 12):

$$\beta_{t,i} = \frac{\Delta E_{t,i,\text{bottom-up}}}{E_{t,i,\text{bottom-up}}} \div \frac{\Delta \Omega_{t,i,\text{bottom-up}}}{\Omega_{t,i,\text{bottom-up}}} \quad (6)$$

where $\Delta E_{t,i,\text{bottom-up}}$ is the emission perturbation (10% reduction in NO_x emissions over the YRD in this work), $\Omega_{t,i,\text{bottom-up}}$ represents the NO₂ TVCDs near the TROPOMI overpass time (06:00 UTC) from the baseline simulation and $\Delta \Omega_{t,i,\text{bottom-up}}$ is the simulation difference after the 10% perturbation in NO_x emissions. Typically, *β* tends to be less than 1 in polluted regions of the YRD because the growth in NO_x emissions consumes hydroxyl radicals and extends the lifetime of NO_x, while in clean areas, growing NO_x emissions reduces the NO_x lifetime, resulting in *β* values greater than 1. Supplementary Fig. 18 shows the average values of regional *β* over the YRD during the major events.

The monthly NO₂ TVCDs from the baseline simulation and RETOMI2 for July, August, September, November and December 2014 (as an example) are shown in Supplementary Fig. 19. Strong correlations were found for all the selected months (*R* > 0.76), while the model performance varied for different months (indicated by different NMBs), in part as a result of the uncertainty in the temporal distribution of NO_x emissions. The bottom-up emission inventory was subject to uncertainties in activity levels, emission factors and the spatiotemporal allocation of emissions, while satellite observations and air quality modeling also introduced errors into the ‘top-down’ estimations.

To further reduce the uncertainty informed by a previous study¹⁴, we computed the a posteriori emission with its errors on a monthly basis using a great likelihood estimation, which combines the top-down estimates and the bottom-up emission inventory by weighting them according to their relative errors. We assumed that the errors in both were lognormally distributed:

$$\ln E_{\text{posteriori}} = \frac{(\ln E_{\text{top-down}})(\ln \varepsilon_{\text{bottom-up}})^2 + (\ln E_{\text{bottom-up}})(\ln \varepsilon_{\text{top-down}})^2}{(\ln \varepsilon_{\text{bottom-up}})^2 + (\ln \varepsilon_{\text{top-down}})^2} \quad (7)$$

$$(\ln \varepsilon_{\text{posteriori}})^{-2} = (\ln \varepsilon_{\text{bottom-up}})^{-2} + (\ln \varepsilon_{\text{top-down}})^{-2} \quad (8)$$

where *E*_{posteriori}, *E*_{top-down} and *E*_{bottom-up} represent the a posteriori, top-down and bottom-up estimates, respectively, and $\varepsilon_{\text{posteriori}}$, $\varepsilon_{\text{bottom-up}}$ and $\varepsilon_{\text{top-down}}$ are the relative errors in the a posteriori, bottom-up and top-down estimates, respectively, which were determined following previous studies^{14,42,43}. Specifically, $\varepsilon_{\text{bottom-up}}$ was determined according to the difference between MEIC and local emission inventories^{44,45}, and $\varepsilon_{\text{bottom-up}}$ is the relative error of the model simulation and satellite data. The former was determined as the difference between simulations with two versions of CMAQ (CMAQ v5.1 and v5.2), while the latter was determined as the difference between daily and monthly averages of NO₂ TVCDs in RETOMI2 for each grid cell.

Decomposing the 7-day moving averages of NO_x emissions into sectors

We combined the a posteriori emissions and sector distribution of bottom-up estimates (MEIC) to obtain the spatiotemporal pattern of NO_x emissions by sector using the method described previously⁴⁶. First, a sector-and-city specific scaling factor was calculated according to the emissions difference between the a posteriori emissions and MEIC for grid cells dominated by a given sector (with the proportion of emissions over 50% in each grid) within the city:

$$\text{scale factor}_{t,s,c} = 1 + \frac{\sum_i (E_{t,i,\text{posteriori}}^{s,c} - E_{t,i,\text{bottom-up}}^{s,c})}{\sum_i (E_{t,i,\text{bottom-up}}^{s,c})} \quad (9)$$

where $E_{t,i,\text{posteriori}}^{s,c}$ and $E_{t,i,\text{bottom-up}}^{s,c}$ are the a posteriori and bottom-up estimates for grid cell *i* in city *c* dominated by sector *s* (such as industry, power or transport) at time *t*, respectively. Note that the residential sector was not considered because of its small contribution to total emissions. Then, the bottom-up emissions were corrected by sector with the scaling factors (equation (10)). Last, we scaled the corrected bottom-up NO_x emissions to be consistent with the a posteriori emissions to minimize the remaining differences. The a posteriori emissions of a given sector were estimated according to the corresponding corrected bottom-up emissions for each grid cell in the city:

$$E_{s,t,i,c,\text{bottom-up,corrected}} = E_{s,t,i,c,\text{bottom-up}} \times \text{scale factor}_{t,s,c} \quad (10)$$

$$E_{s,t,i,c,\text{constrained}} = E_{s,t,i,c,\text{bottom-up,corrected}} \times \frac{E_{t,i,c,\text{posteriori}}}{\sum_s E_{s,t,i,c,\text{bottom-up,corrected}}} \quad (11)$$

where $E_{s,t,i,c,\text{bottom-up,corrected}}$ and $E_{s,t,i,c,\text{bottom-up}}$ represent the corrected and initial bottom-up NO_x emissions from sector *s* for city *c* at time *t*, respectively, and $E_{s,t,i,c,\text{constrained}}$ is the final target NO_x emissions from sector *s* for city *c* at time *t*.

Separating the contributions of emission and meteorological variations to changing NO₂ concentrations

We assessed the contributions of emission and meteorological variations to changing air quality during each major event through simulation experiments based on the a posteriori emissions, informed by previous work⁴⁷. The simulations integrated varying meteorological and emission inputs to quantify their respective influence on changes in NO₂ concentration, including BASE, meteorological change (MET) and emission change (EMIS). The simulation periods are shown in Supplementary Table 6, where P2 is basically equivalent to the main control period of each major event (except 2010 EXPO) and P1 is the time period before P2 with the same duration as P2. The BASE case employed both varying meteorological and emission inputs from P1 to P2, reflecting the actual conditions, MET maintained constant emission levels at the P1 level but applied varying meteorological inputs to evaluate meteorological-induced (MI) changes and EMIS

fixed the meteorological conditions at the P1 level but applied varying emission inputs, allowing the direct determination of emission-induced (EI) changes.

The MI and EI changes can be estimated as follows:

$$MI_{MET} = conc_{P2,MET} - conc_{P1,MET} \quad (12)$$

$$EI_{MET} = conc_{P2,BASE} - conc_{P1,BASE} - MI_{MET} \quad (13)$$

where MI_{MET} and EI_{MET} represent the MI and EI changes estimated on the basis of the results obtained with MET, respectively, $conc_{P1,MET}$ and $conc_{P2,MET}$ represent the average concentrations of NO_2 during P1 and P2 under MET, respectively, and $conc_{P1,BASE}$ and $conc_{P2,BASE}$ represent the average concentrations of NO_2 during P1 and P2 under BASE conditions, respectively. Similarly, the MI and EI changes were also estimated on the basis of EMIS:

$$EI_{EMIS} = conc_{P2,EMIS} - conc_{P1,EMIS} \quad (14)$$

$$MI_{EMIS} = conc_{P2,BASE} - conc_{P1,BASE} - EI_{EMIS} \quad (15)$$

Due to the nonlinear effects of atmospheric chemical systems, the two cases yielded different MI and EI changes. The average of the two cases was used in this study to represent the contribution of emission variation ($contri_{EMIS}$) and meteorological variation ($contri_{MET}$) to NO_2 concentration during the major events:

$$contri_{MET} = \frac{MI}{MI+EI} \times 100 \quad (16)$$

$$contri_{EMIS} = \frac{EI}{MI+EI} \times 100 \quad (17)$$

where MI is the average of MI_{MET} and MI_{EMIS} and EI is the average of EI_{MET} and EI_{EMIS} .

Reporting summary

Further information on research design is available in the Nature Portfolio Reporting Summary linked to this article.

Data availability

The tropospheric NO_2 column data from POMINO, POMINO-TROPOMI and GOME-2 were taken from <http://www.pku-atmos-acm.org/acm-Product.php/> and <https://www.temis.nl/>. Meteorological variables were downloaded from the ERA5 hourly atmospheric reanalysis dataset (accessible at <https://cds.climate.copernicus.eu/datasets/>). Population density data were obtained from WordPop (<https://hub.worldpop.org/geodata/summary?id=44833>). The bottom-up emissions were taken from the Multiple-resolution Emission Inventory for China (<http://www.meicmodel.org>). The data produced in this study (RETOMI2 and the a posteriori emissions of NO_x for the 11 events), as well as the source data for Figs. 1–5, are available via Figshare at <https://figshare.com/s/d8b9b6e8b9f34ab5bdc8> (ref. 49). Source data are provided with this paper.

Code availability

The codes for predicting NO_2 TVCDs using XGBoost and DINEOF and for estimating the a posteriori NO_x emissions are available via Figshare at <https://figshare.com/s/d8b9b6e8b9f34ab5bdc8> (ref. 49).

References

1. Circular of the State Council on Printing Out and Distribution of Action Plan on Air Pollution Prevention and Control Report No. Guofa (2013) 37 (in Chinese) (State Council of the People's Republic of China, 2013); https://www.gov.cn/gongbao/content/2013/content_2496394.htm
2. Circular of the State Council on Printing Out and Distribution of Three-Year Action Plan on Defending the Blue Sky Report No. Guofa (2018) 22 (in Chinese) (State Council of the People's Republic of China, 2018); https://www.gov.cn/gongbao/content/2018/content_5306820.htm
3. Huang, K. et al. How to improve the air quality over megacities in China: pollution characterization and source analysis in Shanghai before, during, and after the 2010 World Expo. *Atmos. Chem. Phys.* **13**, 5927–5942 (2013).
4. Chan, K. L. et al. Observations of tropospheric NO_2 using ground based MAX-DOAS and OMI measurements during the Shanghai World Expo 2010. *Atmos. Environ.* **119**, 45–58 (2015).
5. Huang, Q. et al. Impacts of emission reduction and meteorological conditions on air quality improvement during the 2014 Youth Olympic Games in Nanjing, China. *Atmos. Chem. Phys.* **17**, 13457–13471 (2017).
6. Ding, J. et al. NO_x emission estimates during the 2014 Youth Olympic Games in Nanjing. *Atmos. Chem. Phys.* **15**, 9399–9412 (2015).
7. Wang, Z. et al. Changes in atmospheric composition during the 2014 APEC conference in Beijing. *J. Geophys. Res. Atmos.* **120**, 12695–12707 (2015).
8. Tao, M. H. et al. Contrasting effects of emission control on air pollution in Central China during the 2019 Military World Games based on satellite and ground observations. *Atmos. Res.* **259**, 105657 (2021).
9. Ji, Y. et al. Counteractive effects of regional transport and emission control on the formation of fine particles: a case study during the Hangzhou G20 summit. *Atmos. Chem. Phys.* **18**, 13581–13600 (2018).
10. Cheng, Y. F. et al. Traffic restrictions in Beijing during the Sino-African Summit 2006: aerosol size distribution and visibility compared to long-term in situ observations. *Atmos. Chem. Phys.* **8**, 7583–7594 (2008).
11. Wang, S. X. et al. Quantifying the air pollutants emission reduction during the 2008 Olympic Games in Beijing. *Environ. Sci. Technol.* **44**, 2490–2496 (2010).
12. Huang, K. et al. The 'APEC Blue' phenomenon: regional emission control effects observed from space. *Atmos. Res.* **164**, 65–75 (2015).
13. Zheng, B. et al. Changes in China's anthropogenic emissions and air quality during the COVID-19 pandemic in 2020. *Earth Syst. Sci. Data* **13**, 2895–2907 (2021).
14. Martin, R. V. et al. Global inventory of nitrogen oxide emissions constrained by space-based observations of NO_2 columns. *J. Geophys. Res. Atmos.* **108**, 4537 (2003).
15. Beirle, S. et al. Megacity emissions and lifetimes of nitrogen oxides probed from space. *Science* **333**, 1737–1739 (2011).
16. Beirle, S. et al. Pinpointing nitrogen oxide emissions from space. *Sci. Adv.* **5**, eaax9800 (2019).
17. Kong, H. et al. Considerable unaccounted local sources of NO_x emissions in China revealed from satellite. *Environ. Sci. Technol.* **56**, 7131–7142 (2022).
18. Peng, X. L. et al. Spatially continuous mapping of daily global ozone distribution (2004–2014) with the Aura OMI sensor. *J. Geophys. Res. Atmos.* **121**, 12702–12722 (2016).
19. Boersma, K. F., Eskes, H. J. & Brinksma, E. J. Error analysis for tropospheric NO_2 retrieval from space. *J. Geophys. Res. Atmos.* **109**, D04311 (2004).
20. Boersma, K. F. et al. An improved retrieval of tropospheric NO_2 columns from the Ozone Monitoring Instrument. *Atmos. Meas. Tech.* **4**, 1905–1928 (2011).
21. Liu, M. et al. A new TROPOMI product for tropospheric NO_2 columns over East Asia with explicit aerosol corrections. *Atmos. Meas. Tech.* **13**, 4247–4259 (2020).

22. Li, M. et al. Anthropogenic emission inventories in China: a review. *Natl Sci. Rev.* **4**, 834–866 (2017).
23. Zheng, B. et al. Trends in China's anthropogenic emissions since 2010 as the consequence of clean air actions. *Atmos. Chem. Phys.* **18**, 14095–14111 (2018).
24. Yahya, K. et al. Decadal evaluation of regional climate, air quality, and their interactions over the continental US and their interactions using WRF/Chem version 3.6.1. *Geosci. Model Dev.* **9**, 671–695 (2016).
25. Kang, D. et al. Simulating lightning NO production in CMAQv5.2: performance evaluations. *Geosci. Model Dev.* **12**, 4409–4424 (2019).
26. Lin, J. T. et al. Retrieving tropospheric nitrogen dioxide from the Ozone Monitoring Instrument: effects of aerosols, surface reflectance anisotropy, and vertical profile of nitrogen dioxide. *Atmos. Chem. Phys.* **14**, 1441–1461 (2014).
27. Liu, Y. M. & Wang, T. Worsening urban ozone pollution in China from 2013 to 2017—Part 2: the effects of emission changes and implications for multi-pollutant control. *Atmos. Chem. Phys.* **20**, 6323–6337 (2020).
28. Wang, Y. T. et al. Sustained emission reductions have restrained the ozone pollution over China. *Nat. Geosci.* **16**, 967–974 (2023).
29. Dong, X. Y. et al. Probe into gaseous pollution and assessment of air quality benefit under sector dependent emission control strategies over megacities in Yangtze River Delta, China. *Atmos. Environ.* **79**, 841–852 (2013).
30. Liu, F. et al. Recent reduction in NO_x emissions over China: synthesis of satellite observations and emission inventories. *Environ. Res. Lett.* **11**, 114002 (2016).
31. *Nanjing Winter and Spring Season Air Quality Assurance Control Program Report No. Ningzhengfa (2015) 225* (in Chinese) (The People's Government of Nanjing, People's Republic of China, 2015); http://www.nanjing.gov.cn/zd/gk/201512/t20151229_1056755.html
32. Kong, H. et al. High-resolution (0.05° × 0.05°) NO_x emissions in the Yangtze River Delta inferred from OMI. *Atmos. Chem. Phys.* **19**, 12835–12856 (2019).
33. Liu, M. Y. et al. Improved aerosol correction for OMI tropospheric NO₂ retrieval over East Asia: constraint from CALIOP aerosol vertical profile. *Atmos. Meas. Tech.* **12**, 1–21 (2019).
34. Eskes, H. J. & Boersma, K. F. Averaging kernels for DOAS total-column satellite retrievals. *Atmos. Chem. Phys.* **3**, 1285–1291 (2003).
35. Goldberg, D. L. et al. A top-down assessment using OMI NO₂ suggests an underestimate in the NO_x emissions inventory in Seoul, South Korea, during KORUS-AQ. *Atmos. Chem. Phys.* **19**, 1801–1818 (2019).
36. Gong, P. et al. Finer resolution observation and monitoring of global land cover: first mapping results with Landsat TM and ETM+ data. *Int. J. Remote Sens.* **34**, 2607–2654 (2013).
37. Tian, X. et al. Long-term observations of tropospheric NO₂, SO₂ and HCHO by MAX-DOAS in Yangtze River Delta area, China. *J. Environ. Sci.* **71**, 207–221 (2018).
38. He, Q. et al. Spatially and temporally coherent reconstruction of tropospheric NO₂ over China combining OMI and GOME-2B measurements. *Environ. Res. Lett.* **15**, 125011 (2020).
39. Song, S. K. et al. Effects of natural and anthropogenic emissions on the composition and toxicity of aerosols in the marine atmosphere. *Sci. Total Environ.* **806**, 150928 (2022).
40. Alvera-Azcárate, A. et al. Reconstruction of incomplete oceanographic data sets using empirical orthogonal functions: application to the Adriatic Sea surface temperature. *Ocean Model.* **9**, 325–346 (2005).
41. Yang, J. Z. et al. Co-benefits of carbon and pollution control policies on air quality and health till 2030 in China. *Environ. Int.* **152**, 683–693 (2021).
42. Zhao, C. & Wang, Y. H. Assimilated inversion of NO_x emissions over east Asia using OMI NO₂ column measurements. *Geophys. Res. Lett.* **36**, L06805 (2009).
43. Qu, Z. et al. Global distribution of methane emissions: a comparative inverse analysis of observations from the TROPOMI and GOSAT satellite instruments. *Atmos. Chem. Phys.* **21**, 14159–14175 (2021).
44. An, J. Y. et al. Emission inventory of air pollutants and chemical speciation for specific anthropogenic sources based on local measurements in the Yangtze River Delta region, China. *Atmos. Chem. Phys.* **21**, 2003–2025 (2021).
45. Gu, C. et al. High-resolution regional emission inventory contributes to the evaluation of policy effectiveness: a case study in Jiangsu Province, China. *Atmos. Chem. Phys.* **23**, 4247–4269 (2023).
46. Zheng, B. et al. Satellite-based estimates of decline and rebound in China's CO₂ emissions during COVID-19 pandemic. *Sci. Adv.* **6**, eabd4998 (2020).
47. Kong, L. et al. Unbalanced emission reductions of different species and sectors in China during COVID-19 lockdown derived by multi-species surface observation assimilation. *Atmos. Chem. Phys.* **23**, 6217–6240 (2023).
48. Xu, X. China's Multi-year Provincial Administrative Division Boundary Data (Resource and Environment Science and Data Center, Institute of Geographic Sciences and Natural Resources Research, Chinese Academy of Sciences, 2023); <https://doi.org/10.12078/2023010103>
49. Wang, H. et al. Source data and code for research 'Declining short-term emission control opportunity for major events in Chinese cities'. *Figshare* <https://figshare.com/s/d8b9b6e8b9f34ab5bdc8> (2025).

Acknowledgements

We acknowledge the free use of tropospheric NO₂ column data from the POMINO, POMINO-TROPOMI and GOME-2 sensors from <http://www.pku-atmos-acm.org/acmProduct.php/> and <https://www.temis.nl/>. We also thank the data support from the National Earth System Science Data Center, National Science and Technology Infrastructure of China (<http://www.geodata.cn>). This work was supported by the National Key Research and Development Program of China (2023YFC3709802, Y.Z.) and the National Natural Science Foundation of China (42177080, Y.Z.).

Author contributions

Conceptualization and methodology: H.W. and Y.Z.; formal analysis and investigation: H.W. and Y.Z.; writing (original draft): H.W. and Y.Z.; writing (review and editing): all authors; visualization: H.W.; code method support: H.W., Q.H., H.K., K.Q. and J.L.; data support: J.L. and B.Z.; supervision and project administration: Y.Z.

Competing interests

The authors declare no competing interests.

Additional information

Supplementary information The online version contains supplementary material available at <https://doi.org/10.1038/s44284-025-00233-x>.

Correspondence and requests for materials should be addressed to Yu Zhao.

Peer review information *Nature Cities* thanks Daiwen Kang, Minghao Qiu and the other, anonymous, reviewer(s) for their contribution to the peer review of this work.

Reprints and permissions information is available at www.nature.com/reprints.

Publisher's note Springer Nature remains neutral with regard to jurisdictional claims in published maps and institutional affiliations.

Springer Nature or its licensor (e.g. a society or other partner) holds exclusive rights to this article under a publishing agreement with

the author(s) or other rightsholder(s); author self-archiving of the accepted manuscript version of this article is solely governed by the terms of such publishing agreement and applicable law.

© The Author(s), under exclusive licence to Springer Nature America, Inc. 2025

Reporting Summary

Nature Portfolio wishes to improve the reproducibility of the work that we publish. This form provides structure for consistency and transparency in reporting. For further information on Nature Portfolio policies, see our [Editorial Policies](#) and the [Editorial Policy Checklist](#).

Statistics

For all statistical analyses, confirm that the following items are present in the figure legend, table legend, main text, or Methods section.

- | n/a | Confirmed |
|-------------------------------------|--|
| <input type="checkbox"/> | <input checked="" type="checkbox"/> The exact sample size (n) for each experimental group/condition, given as a discrete number and unit of measurement |
| <input checked="" type="checkbox"/> | <input type="checkbox"/> A statement on whether measurements were taken from distinct samples or whether the same sample was measured repeatedly |
| <input checked="" type="checkbox"/> | <input type="checkbox"/> The statistical test(s) used AND whether they are one- or two-sided
<i>Only common tests should be described solely by name; describe more complex techniques in the Methods section.</i> |
| <input checked="" type="checkbox"/> | <input type="checkbox"/> A description of all covariates tested |
| <input checked="" type="checkbox"/> | <input type="checkbox"/> A description of any assumptions or corrections, such as tests of normality and adjustment for multiple comparisons |
| <input type="checkbox"/> | <input checked="" type="checkbox"/> A full description of the statistical parameters including central tendency (e.g. means) or other basic estimates (e.g. regression coefficient) AND variation (e.g. standard deviation) or associated estimates of uncertainty (e.g. confidence intervals) |
| <input checked="" type="checkbox"/> | <input type="checkbox"/> For null hypothesis testing, the test statistic (e.g. F , t , r) with confidence intervals, effect sizes, degrees of freedom and P value noted
<i>Give P values as exact values whenever suitable.</i> |
| <input type="checkbox"/> | <input checked="" type="checkbox"/> For Bayesian analysis, information on the choice of priors and Markov chain Monte Carlo settings |
| <input checked="" type="checkbox"/> | <input type="checkbox"/> For hierarchical and complex designs, identification of the appropriate level for tests and full reporting of outcomes |
| <input checked="" type="checkbox"/> | <input type="checkbox"/> Estimates of effect sizes (e.g. Cohen's d , Pearson's r), indicating how they were calculated |

Our web collection on [statistics for biologists](#) contains articles on many of the points above.

Software and code

Policy information about [availability of computer code](#)

- | | |
|-----------------|---|
| Data collection | Internet Download Manager (IDM) 6.36 (for downloading satellite data) |
| Data analysis | We used a coupled Weather Research and Forecasting-Community Multi-scale Air Quality (WRF-CMAQ, version:WRFv3.9.1, CMAQv5.2 and v5.1) for inverse modeling. We used python version 3.9 for conducting the XGBoost, and matlab version 9.13.0 (R2022b) for conducting the DINEOF. The relevant code is provided in Figshare (https://figshare.com/s/d8b9b6e8b9f34ab5bdc8). |

For manuscripts utilizing custom algorithms or software that are central to the research but not yet described in published literature, software must be made available to editors and reviewers. We strongly encourage code deposition in a community repository (e.g. GitHub). See the Nature Portfolio [guidelines for submitting code & software](#) for further information.

Data

Policy information about [availability of data](#)

All manuscripts must include a [data availability statement](#). This statement should provide the following information, where applicable:

- Accession codes, unique identifiers, or web links for publicly available datasets
- A description of any restrictions on data availability
- For clinical datasets or third party data, please ensure that the statement adheres to our [policy](#)

Data publicly available in a repository: The free use of tropospheric NO₂ column data from the POMINO, POMINO-TROPOMI and GOME-2 sensor from <http://www.pku-atmos-acm.org/acmProduct.php/> and <https://www.temis.nl/>. Meteorological variables were downloaded from the ERA5 hourly atmospheric reanalysis

dataset (accessible online through <https://cds.climate.copernicus.eu/cdsapp#!/home>). Population density data were obtained from WordPop (<https://hub.worldpop.org/geodata/summary?id=44833>). The bottom-up emissions were taken from Multiple-resolution Emission Inventory for China (MEIC; <http://www.meicmodel.org>). The authors declare that the data supporting the findings of this study are available within the paper, its supplementary information files, and the figshare (<https://figshare.com/s/d8b9b6e8b9f34ab5bdc8>).

Research involving human participants, their data, or biological material

Policy information about studies with [human participants or human data](#). See also policy information about [sex, gender \(identity/presentation\), and sexual orientation](#) and [race, ethnicity and racism](#).

Reporting on sex and gender

Reporting on race, ethnicity, or other socially relevant groupings

Population characteristics

Recruitment

Ethics oversight

Note that full information on the approval of the study protocol must also be provided in the manuscript.

Field-specific reporting

Please select the one below that is the best fit for your research. If you are not sure, read the appropriate sections before making your selection.

Life sciences Behavioural & social sciences Ecological, evolutionary & environmental sciences

For a reference copy of the document with all sections, see nature.com/documents/nr-reporting-summary-flat.pdf

Ecological, evolutionary & environmental sciences study design

All studies must disclose on these points even when the disclosure is negative.

Study description

Research sample

Sampling strategy

Data collection http://www.pku-atmos-acm.org/acmProduct.php/ and <https://www.temis.nl/>. Meteorological variables were downloaded from the ERA5 hourly atmospheric reanalysis dataset (accessible online through <https://cds.climate.copernicus.eu/cdsapp#!/home>). Population density data were obtained from WordPop (<https://hub.worldpop.org/geodata/summary?id=44833>). The bottom-up emissions were taken from Multiple-resolution Emission Inventory for China (MEIC; <http://www.meicmodel.org>). See Method and SI for more details."/>

Timing and spatial scale

Data exclusions

Reproducibility

Randomization

Blinding

Did the study involve field work? Yes No

Reporting for specific materials, systems and methods

We require information from authors about some types of materials, experimental systems and methods used in many studies. Here, indicate whether each material, system or method listed is relevant to your study. If you are not sure if a list item applies to your research, read the appropriate section before selecting a response.

Materials & experimental systems

n/a	Involvement in the study
<input checked="" type="checkbox"/>	<input type="checkbox"/> Antibodies
<input checked="" type="checkbox"/>	<input type="checkbox"/> Eukaryotic cell lines
<input checked="" type="checkbox"/>	<input type="checkbox"/> Palaeontology and archaeology
<input checked="" type="checkbox"/>	<input type="checkbox"/> Animals and other organisms
<input checked="" type="checkbox"/>	<input type="checkbox"/> Clinical data
<input checked="" type="checkbox"/>	<input type="checkbox"/> Dual use research of concern
<input checked="" type="checkbox"/>	<input type="checkbox"/> Plants

Methods

n/a	Involvement in the study
<input checked="" type="checkbox"/>	<input type="checkbox"/> ChIP-seq
<input checked="" type="checkbox"/>	<input type="checkbox"/> Flow cytometry
<input checked="" type="checkbox"/>	<input type="checkbox"/> MRI-based neuroimaging

Plants

Seed stocks

No plant was applied in this work.

Novel plant genotypes

No plant genotype was applied in this work.

Authentication

Not applicable.